

Dual-Anion Zn²⁺ Electrolytes having Sulfate and Triflate for Highly Reversible and Stable Operation of Zinc Metal Anode

Aditya Ranjan Pati, Sangram Keshari Mohanty, Sri Charan Reddy, Chetan Lakshman, Sung-Ho Jin, and Hyun Deog Yoo*

Zinc-ion batteries (ZIBs) have emerged as a viable option for energy storage applications in response to the growing need for energy due to their low cost, acceptable energy density, high natural abundance, high safety, and high volumetric and gravimetric capacity due to the divalent nature of Zn²⁺. However, it is necessary to extend the longevity of ZIBs by optimizing Zinc-ion electrolytes for the stable operation of the Zn metal anode, where passivation layers suppress its corrosion and dendritic growth. Herein, an electrochemical quartz-crystal microbalance analysis is conducted to characterize passivation layers formed during the deposition/dissolution of zinc metal in aqueous electrolyte solutions of zinc sulfate (ZnSO₄), zinc triflate

(Zn(OTf)₂), and their mixture at varied ratios as dual-salt hybrid electrolytes. The varied anionic compositions result in different passivation behaviors with characteristic reversibility and potential-dependency. Specifically, mixed electrolytes exhibit more stable and efficient operation of the zinc metal anode by the formation of passivation layers with balanced robustness and reversibility. The mass-per-electron value is close to the ideal value for the optimized electrolyte solution, evidencing the importance of electrolyte formulation for advanced ZIB technologies toward safer and more energy-dense aqueous energy storage devices.

1. Introduction

Amid escalating concerns over environmental degradation, energy shortages, and safety challenges, the development of eco-friendly and high-performance energy storage systems (ESS) has become imperative, motivating scientists to diversify battery technologies for sustainable energy storage across various sectors.^[1–3] In the landscape of battery development, Li-ion batteries have secured the leading position, primarily attributed to the high energy density that is suitable for portable electronics and electric vehicles.^[4–7] However, to address broader challenges in modern energy infrastructure, large-scale grid

storage systems are needed, for which the rechargeable Zn-ion battery has emerged as a promising candidate.^[8–11] Aqueous zinc-ion batteries (AZBs) offer a compelling alternative to Li-ion systems by addressing challenges related to resource scarcity, safety, cost, and scalability. With high intrinsic safety, a high gravimetric and volumetric capacity due to the multivalent nature of Zn²⁺, and a low redox potential (−0.76 V vs. standard hydrogen electrode (SHE)), Zn metal enables AZBs to meet the growing demands of grid-scale and sustainable energy storage.^[12–15] Despite their numerous advantages, AZBs encounter several critical challenges, including a limited operating voltage window, continued zinc corrosion, formation of side products, and the absence of a dense and stable passivation layer, whereby the Zn metal anode experiences dendrite formation and shortened cycling stability.^[16,17] Recently, researchers have employed a range of approaches to addressing issues for AZBs, including electrode regulation, forming an artificial solid-electrolyte interphase (SEI), separator selection, and optimized binders.^[18–23] Among these, electrolyte engineering has emerged as a pivotal approach, playing a crucial role in broadening the electrochemical window, enhancing ionic conductivity, suppressing side reactions, and stabilizing Zn plating/stripping processes, thereby serving as a key strategy for achieving long-term cycling stability and advancing the practical application of aqueous Zn-based batteries.^[24–26] In this context, the identification and optimization of effective aqueous electrolytes have become critical, with particular emphasis on selecting salts that offer a balance between electrochemical stability and compatibility with Zn metal anodes.

A. R. Pati, S. K. Mohanty, S. C. Reddy, H. D. Yoo
Department of Chemistry and Institute for Future Earth
Pusan National University

Busan 46241, Republic of Korea
E-mail: hyundeog.yoo@pusan.ac.kr

C. Lakshman, S.-H. Jin
Department of Chemistry Education
Graduate Department of Chemical Materials
Sustainable Utilization of Photovoltaic Energy Research Center (ERC)
Institute for Plastic Information and Energy Materials

Pusan National University
Busan 46241, Republic of Korea

 Supporting information for this article is available on the WWW under <https://doi.org/10.1002/batt.202500371>

 © 2025 The Author(s). *Batteries & Supercaps* published by Wiley-VCH GmbH. This is an open access article under the terms of the Creative Commons Attribution License, which permits use, distribution and reproduction in any medium, provided the original work is properly cited.

Among various aqueous electrolytes explored for AZBs, zinc sulfate (ZnSO_4 ; ZS) and zinc triflate ($\text{Zn}(\text{OTf})_2$; also known as trifluoromethanesulfonate; ZT) have gained significant attention due to their distinctive electrochemical properties after being first introduced by Yamamoto et al. and Liu, J. et al. respectively.^[27,28] ZnSO_4 -based electrolytes are widely favored for their cost-effectiveness, environmentally benign nature, and mildly acidic nature, which offers improved cycling stability than conventional alkaline electrolytes, making them attractive for scalable ESS.^[29] However, the narrow electrochemical stability window (ESW) of sulfate-based electrolytes makes them susceptible to side reactions, such as the hydrogen evolution reaction (HER), leading to battery swelling, and the formation of irreversible byproducts like zinc hydroxide sulfate (ZHS; $\text{Zn}_4(\text{OH})_6\text{SO}_4 \cdot n\text{H}_2\text{O}$) that eventually leads to cell failure. Additionally, the sulfate electrolyte promotes dendrite growth and 'dead zinc' due to inhomogeneous nucleation, which consumes active Zn and electrolyte, ultimately resulting in low Zn plating/stripping efficiency and an increased risk of short-circuiting.^[30,31] In contrast, $\text{Zn}(\text{OTf})_2$ electrolytes, owing to the large coordinating and hydrophobic nature of triflate anions, effectively suppress water activity, mitigate HER, and promote interfacial stability, thereby facilitating more uniform and reversible Zn deposition.^[32,33] Nevertheless, challenges such as elevated cost, limited commercial availability, moderate Zn^{2+} solubility, and significant environmental concerns associated with fluorine content restrict their widespread use in practical battery applications.^[34,35]

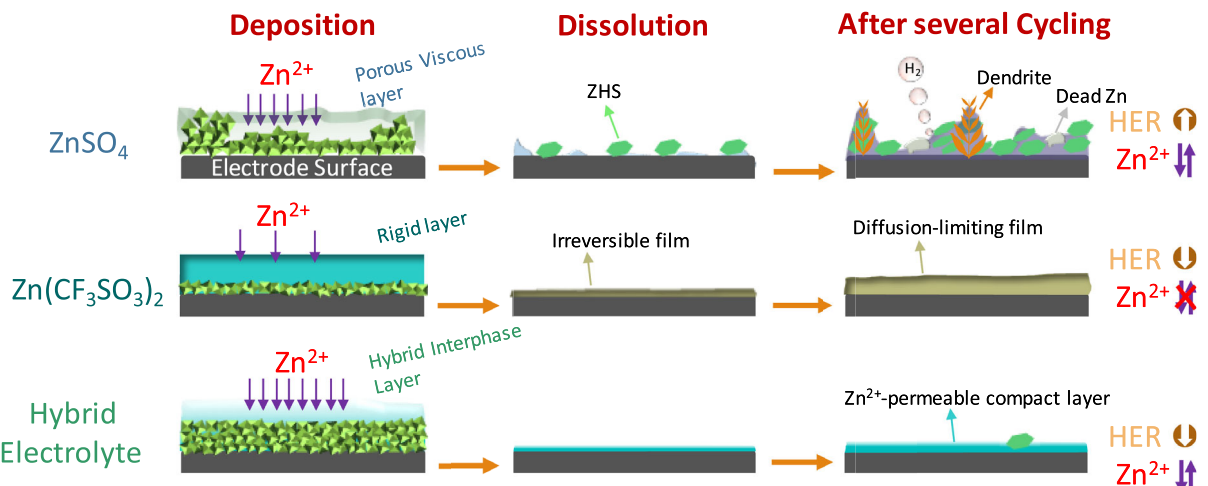
To overcome these individual shortcomings of conventional single-salt electrolytes, rationally designing a dual-salt hybrid electrolyte (DSHE) has emerged as a promising strategy, as demonstrated by several research groups, to synergistically regulate Zn plating/stripping dynamics and enhance interfacial stability.^[36,37] Although dual-salt electrolytes offer the potential to simultaneously suppress side reactions, improve ionic conductivity, and promote more uniform Zn deposition, a fundamental understanding of the interfacial behavior remains critical as essential electrochemical processes occur at the electrode-electrolyte interface, which ultimately governs the cell's cycling stability.^[38,39] These processes are inherently complex and challenging to elucidate in the absence of in situ characterization techniques. In this context, electrochemical quartz-crystal microbalance (EQCM) serves as a highly sensitive tool for real-time monitoring of mass changes (Δm) and interfacial viscoelasticity, as reflected by motional resistance variations (ΔR_m), during electrochemical processes. This technique enables a detailed investigation of Zn deposition/dissolution behavior and passivation layer formation under varying electrolyte conditions, offering valuable insights into electrode-electrolyte interfacial dynamics.^[40] The underlying principle of EQCM is based on the fundamental relationship between frequency change (Δf) and mass change by Sauerbrey through the equation $\Delta f = -C_f \Delta m$,^[41] under the assumption that the deposited mass forms a thin, rigid, and uniformly distributed film. However, the pioneering work of Nomura and Okuhara in applying quartz-crystal microbalance (QCM) to liquid-phase environments revealed that Δf is also influenced by the viscosity of the surrounding medium.^[42] In real

electrolyte environments, metal deposition is not purely rigid but often involves associated solvent molecules through direct hydration, solvation, or entrapment within the adsorbed layer, contributing additional dynamic mass. Viscoelastic films, due to their flexible, gel-like nature, partially decouple from the surface acoustic wave generated by the oscillating crystal, as these layers cannot oscillate coherently with the crystal. This decoupling results in energy dissipation due to damping effects; thus, accurate characterization of the electrode-electrolyte interface requires simultaneous measurement of both mass change (Δm) and motional resistance (ΔR_m), rather than relying solely on frequency shift.^[43]

In this work, a series of DSHEs composed of ZnSO_4 and $\text{Zn}(\text{OTf})_2$ at various concentration ratios was employed by employing electrolyte engineering strategies to address the inherent limitations of conventional single-salt aqueous electrolytes and achieved an increased ion transport efficiency with improved Zn plating/stripping performance. To gain a comprehensive understanding of the interfacial phenomena associated with electrolyte environments, EQCM was employed as the primary investigative tool to monitor mass changes and viscoelastic responses in real-time during both voltammetric and galvanostatic cycling. Hybrid electrolytes with higher triflate concentrations exhibited promising results by forming distinct and enhanced interfacial characteristics inherited from both sulfate and triflate anions, as evidenced by near-ideal mass per electron (MPE) trends and improved mass reversibility. In addition to EQCM, complementary characterizations including X-ray diffraction (XRD), scanning electron microscopy integrated with energy-dispersive spectroscopy (SEM-EDS), and others were conducted to gain deeper insights into the surface and interfacial properties. Finally, to assess the practical applicability of the optimized electrolyte system, $\text{Zn}||\text{Zn}$ symmetric and $\text{Cu}||\text{Zn}$ asymmetric cells were assembled and systematically tested for their electrochemical performance and cycling durability.

2. Results and Discussion

As illustrated in the schematic diagram (Scheme 1), anion identity and solvation structure critically influence Zn deposition behavior and interfacial stability. In ZnSO_4 -based electrolytes, highly hydrated SO_4^{2-} anions promote solvent-separated ion pairs, increasing water activity and facilitating parasitic reactions such as HER and ZHS formation.^[44] The resulting porous and viscoelastic ZHS layer induces nonuniform Zn^{2+} deposition, leading to dendrite growth and dead Zn.^[45,46] Conversely, in $\text{Zn}(\text{CF}_3\text{SO}_3)_2$ electrolytes, bulky and hydrophobic CF_3SO_3^- anions form contact ion pairs (CIPs) with Zn^{2+} , reducing water activity and enabling compact, uniform Zn deposition.^[47,48] Their strong interfacial adsorption forms a rigid passivation layer that suppresses HER but restricts Zn^{2+} transport and mass utilization. The DSHE combines the advantages of both systems, yielding a stable, ion-conductive interphase that balances passivation and ion mobility, enhancing Zn reversibility and long-term cycling performance.



Scheme 1. Schematic representation of surface film evolution observed during Zn deposition, dissolution, and after prolonged cycling, as derived from EQCM analysis using various electrolytes.

Cyclic voltammetry (CV) analysis (Figure 1a, S1a, Supporting Information) revealed that the sulfate, triflate-based, and hybrid electrolytes displayed distinct anodic and cathodic peak intensities, indicating variations in their Zn-ion deposition and dissolution kinetics. The pure triflate-based electrolyte demonstrates the lowest current density (1.28 mA cm^{-2}) and the highest overpotential for Zn deposition, signifying that the sluggish kinetics may be due to the bulky CF_3SO_3^- anion-solvated Zn^{2+} cations forming CIPs among all electrolytes.^[33] However, the hybrid electrolytes, 0.25 M ZS + 1.25 M ZT, exhibit the highest current densities (3.4 mA cm^{-2}) and lower overpotentials compared to the

pure ones, likely due to their enhanced ionic conductivity, which facilitates more efficient ion migration and improved reaction kinetics.

Figure 1b and S1b, Supporting Information, represent the coulombic efficiency (CE) during the first voltammetric cycling, where the pure zinc triflate electrolyte showed the lowest CE of 95.6%, while the 0.25 M ZS + 1.25 M ZT electrolyte achieves the highest value of 97.4%. During five consecutive CV cycles (Figure 1c, S1c, Supporting Information), all electrolytes, except 2.5 M ZT, exhibited a stable CE of $\approx 97\%$, revealing good reversibility of Zn plating/stripping on the electrode. In contrast, the CE

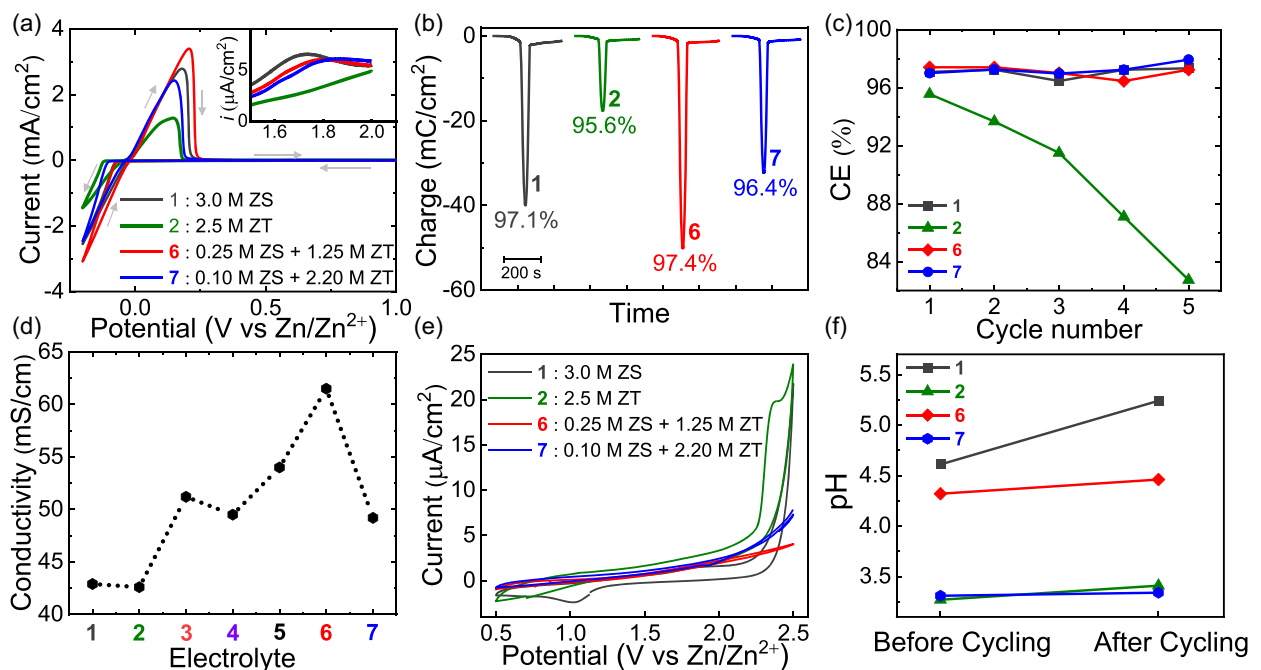


Figure 1. Electrochemical investigation of different electrolytes: a) cyclic voltammograms depicting electrochemical behavior with the zoomed-in view in the inset, b) charge versus time profiles with CE value of first cycle, c) CE as a function of cycle number, d) conductivity measurement at 25°C for all electrolytes, e) ESW measurement, f) pH change of different electrolytes before and after electrochemical cycling.

of the pure triflate electrolyte declined from 96% to 82%, suggesting the formation of an irreversible layer, which is consistent with the EQCM results. From the conductivity measurements (Figure 1d), both pure electrolytes showed nearly identical conductivities of 43 mS cm^{-1} . However, 0.25 M ZS + 1.25 M ZT demonstrated the highest conductivity of 61.5 mS cm^{-1} among all electrolytes, highlighting enhanced ionic migration, which is expected to contribute to improved electrochemical performance. The overall increase in conductivity with rising ZT content (from electrolyte 3 to 6) is attributed to the triflate anion's large size, monovalent charge, and hydrophobic CF_3 group, which reduce hydration, enhance ion dissociation, and increase anion mobility compared to SO_4^{2-} , thereby generating more mobile charge carriers.^[49,50] Notably, this conductivity is significantly higher than that typically observed in nonaqueous electrolytes ($1\text{--}10 \text{ mS cm}^{-1}$).^[51,52] High-concentrated electrolytes, including pure and 0.10 M ZS + 2.2 M ZT, had less conductivity due to enhanced ionic interactions, limiting ion mobility inside the system.

Electrochemical stability window (ESW) and Zn^{2+} transference number (t_+) measurements were conducted to further assess the electrochemical performance of the electrolytes. ESW was evaluated by CV (Figure 1e), where hybrid electrolytes (6 and 7) exhibited lower anodic currents at high potential (2.5 V) compared to pure systems, indicating improved stability, likely due to mixed Zn^{2+} coordination. Transference numbers were estimated using the Bruce–Vincent method,^[53] and the t_+ values decreased from 0.22 to 0.10 as ZT content increased (Figure S3, Table S1, Supporting Information). This tendency is consistent with the dominant anion mobility of OTf^- , as previously discussed in the context of the conductivity trend.

To further substantiate HER suppression in hybrid electrolytes, pH measurements before and after cycling were performed

(Figure 1f, Table S2). Pure ZS showed the highest pH increase ($\Delta\text{pH} = 0.63$), indicating substantial H_2 evolution, while ZT exhibited a smaller change ($\Delta\text{pH} = 0.14$) likely due to the formation of a dense interfacial layer that reduces water activity at the electrode surface. Notably, hybrid electrolytes (6 and 7) showed minimal pH shifts ($\Delta\text{pH} = 0.05$ and 0.04), supporting the role of dual-anion coordination in mitigating water decomposition through the formation of a distinct interfacial layer.

To elucidate the Zn deposition and dissolution behavior along with viscoelastic properties under different electrolyte conditions, Figure 2 provides a combined analysis of mass change (Δm) and motional resistance variation (ΔR_m) on the QCM electrode during the initial potential scan for the four electrolytes. Focusing on mass change curves, 3 M ZS illustrates a potential-dependent surface film formation, whereas 2.5 M ZT forms an irreversible surface film on the electrode that persists despite potential changes, unlike the sulfate-based electrolyte, which undergoes dissolution. In contrast to pure electrolytes, the hybrid electrolytes showed improved reversibility in Zn plating/stripping, indicating the mitigation of byproduct generation. This improved reversibility can be beneficial for achieving stable and efficient Zn cycling.

By analyzing the ΔR_m trends across different electrolytes, a more accurate assessment of surface behavior before and after metal deposition/dissolution was estimated. 3.0 M ZS showed a higher ΔR_m value, emphasizing a highly viscoelastic film formation, likely resulting from the formation of a porous and loosely adhered ZHS layer on the Pt electrode,^[46] which facilitates more Zn deposition, as shown by the high Δm value. In contrast, 2.5 M ZT showed a significantly lower ΔR_m value, confirming the development of a rigid surface layer over the electrode.^[54] This behavior may be attributed to the triflate anion's robust adsorption capability with Zn^{2+} due to CIPs formation, which may

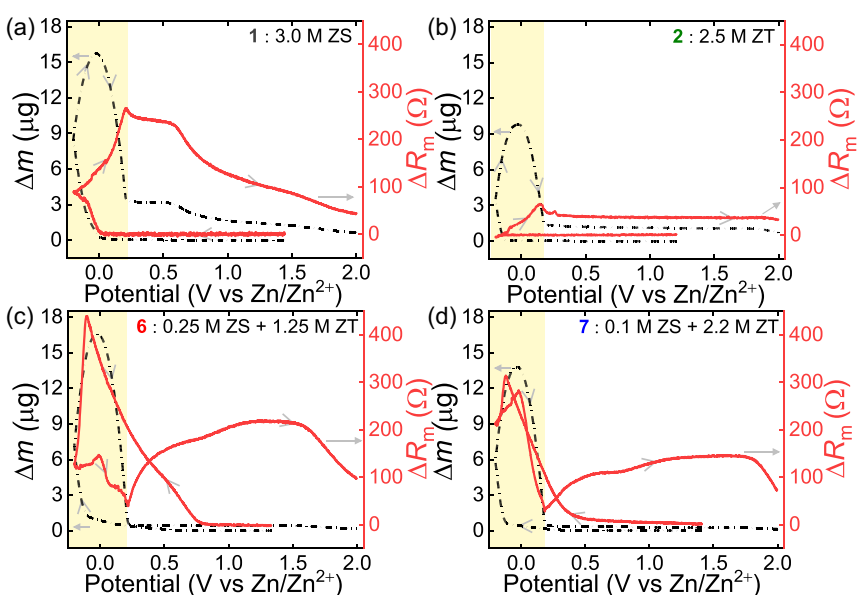


Figure 2. Combined analysis of mass deposition/ dissolution of Zn with motional resistance changes over an EQCM electrode during electrochemical cycling using different electrolytes: a) 1, b) 2, c) 6, and d) 7.

prevent further Zn nucleation and lead to reduced mass deposition. The persistent rise in motional resistance in both electrolytes after Zn dissolution suggests the formation of a viscous interfacial environment, originating from interactions between Zn^{2+} and coordinating anions, forming complex ions like ZHS and zinc triflate hydroxy hydrate (ZOTH; $Zn_xOTf_y(OH)_{2x-y} \cdot nH_2O$).^[55,56] This layer appears to dissolve gradually at higher potentials in 3.0 M ZS, whereas in 2.5 M ZT it remains largely unchanged, reflecting its irreversible nature.

Hybrid electrolytes (Figure 2c,d) showed distinct interfacial behaviors during Zn deposition/dissolution than pure ones, as evidenced by different ΔR_m trends. In EQCM, Δm primarily reflects rigid mass changes at the electrode surface, whereas ΔR_m is sensitive to energy dissipation caused by viscoelastic or loosely bound interfacial species. Decoupling between these signals indicates the formation of nonrigid, dissipative interfacial layers—such as solvated ion adsorbates or hydrated, gel-like films, that do not significantly contribute to mass loading.^[57] In pure electrolytes, ΔR_m increased concurrently with mass deposition, displaying rough surface formation. In contrast, hybrid electrolytes showed a rise in ΔR_m prior to any noticeable mass change, indicating the formation of a viscoelastic predeposition interfacial layer. This phenomenon likely arises due to Zn^{2+} being coordinated simultaneously by SO_4^{2-} and OTf^- anions. The disparity in anion charge and coordination strength creates an asymmetric coordination environment around Zn^{2+} , promoting the formation of larger and more complex solvation structures. This modified coordination environment can give rise to loosely packed interfacial layers, particularly near the point of zero charge (≈ 0.8 V vs Zn/Zn^{2+}), where Zn²⁺ accumulation near the electrode surface is

electrostatically favorable. Such layers enhance mechanical energy dissipation, leading to elevated ΔR_m prior to rigid Zn nucleation, and may ultimately facilitate more uniform and compact Zn deposition.

As the potential approaches 0 V versus Zn/Zn^{2+} , ΔR_m begins to decrease while Δm increases, marking a transition to a more rigid, compact Zn layer. We interpret this as the formation of a Zn—permeable compact interphase, mechanically stable yet allowing ionic transport. The compactness is primarily attributed to OTf^- -based coordination, while the sulfate component contributes to ion permeability. A subsequent slight rise in ΔR_m suggests localized dendrite initiation or surface roughness atop the rigid Zn layer. Upon dissolution, ΔR_m initially decreases, pointing out the desolvation of the irregular surface over the rigid layer, followed by an increase after complete Zn removal, consistent with the formation of a viscous interfacial environment as discussed previously. This behavior was also observed in other hybrid electrolytes (Figure S4, Supporting Information), supporting the role of asymmetric coordination environment in dual-anion electrolytes for modulating interfacial structure. This interfacial behavior may contribute to improved electrochemical performance by promoting uniform Zn deposition and suppressing parasitic reactions. To better visualize the dynamic relationship between Δm and ΔR_m during Zn deposition and dissolution, their time-resolved profiles are presented in Figure S3, Supporting Information.

The mass per electron (mpe) values for the initial Zn plating/stripping cycle are displayed in Figure 3, providing insights into deposition efficiency and reaction pathways. Complementary to CE, mpe reveals mass reversibility and interfacial film formation

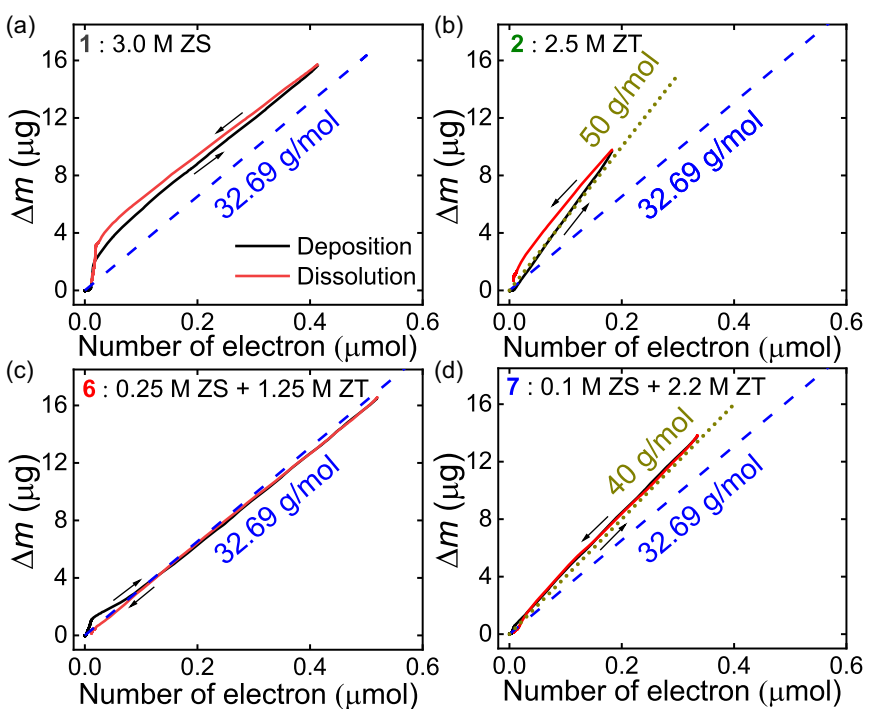


Figure 3. Mass per electron profile for different electrolytes during redox cycling: a) 1, b) 2, c) 6, and d) 7.

mechanisms, where hysteresis in the mpe curve indicates asymmetric mass changes during plating and stripping, often arising from partially reversible or parasitic processes. The initial deviation from the ideal mpe (32.69 g mol^{-1}) value observed in 3 M ZS at the onset of Zn deposition and the end of dissolution, along with the presence of hysteresis, enlightens the occurrence of side reactions and potential-dependent surface film formation, probably involving hydrated byproducts such as ZHS on the electrode. The calculated mpe value for 2.5 M ZT is 50 g mol^{-1} , which aligns with the theoretical mpe value for Zn(OH)_2 ($m/z 50 \text{ g mol}^{-1}$), suggesting the possible formation of Zn(OH)_2 during initial cycling.^[58] Electrolyte 6 exhibited a mpe curve close to the ideal value, conveyed predominantly Zn plating/stripping with minimal side reactions. In contrast, electrolyte 7 demonstrated good reversibility, though a deviation from the ideal value, demonstrating the formation of ZnO , similar to the behavior observed in pure triflate electrolytes. As shown in Figure S5, Supporting Information, electrolytes 3, 4, and 5 exhibited greater deviation from the ideal mpe value along with pronounced hysteresis, indicating increased parasitic reactions compared to the more stable and reversible behavior observed in electrolytes 6 and 7. Furthermore, in pure electrolytes, the higher mpe value during the cathodic sweep than the anodic sweep indicates side reactions, whereas hybrid electrolytes 6 and 7 showed a reversible mpe trend, exhibiting good efficiency and better suitability for electrolyte selection.

The mass change (Δm) trends during the initial two consecutive cycles for the electrolytes are shown in Figure 4 and S6, Supporting Information. The continuous formation of irreversible byproducts on the electrode, resulting from persistent side

reactions in pure electrolytes, led to a progressive increase in irreversibility over cycling. In contrast, hybrid electrolytes, especially in 6 and 7, exhibited a minimal increase in Δm , demonstrating effective mitigation of parasitic reactions and improved Zn reversibility. A similar trend of irreversibility was observed in subsequent cycles (Figure S7 & S8, Supporting Information), with a reduced deposition/dissolution amount, which may be attributed to the higher scan rate (25 mV s^{-1}). By considering the high mass reversibility and near-ideal mpe, electrolytes 6 and 7 were chosen as representative electrolytes among the hybrid electrolytes.

To analyze the amount of Zn plating/stripping over an extended charge-discharge process and to evaluate the overpotential offered by different electrolytes, galvanostatic cycling with potential limitation (GCPL) was conducted following multiple voltammetric cycles. Figure 5 and S9, Supporting Information represent the GCPL profiles for four consecutive cycles, where Zn was deposited for 6 min at a current density of -0.1 mA and subsequently dissolved at $+0.1 \text{ mA}$, with a cutoff potential of 2 V versus Zn/Zn^{2+} . The galvanostatic voltage profile shown in Figure 5a suggests that, while deposition, pure triflate electrolyte showed a higher overpotential than others due to the sluggish kinetics aligned with the CV results. A steep voltage rise was observed in 2.5 M ZT during the charging step, exhibiting the development of a rigid byproduct layer on the electrode surface, which may likely hinder Zn dissolution and lead to high overpotential. This behavior persisted over successive GCPL cycles, suggesting no significant change in surface features with continued cycling, as further corroborated by reduced mass deposition behavior in Δm versus time analysis. However, other electrolytes, especially the hybrid electrolytes, showed a gradual voltage

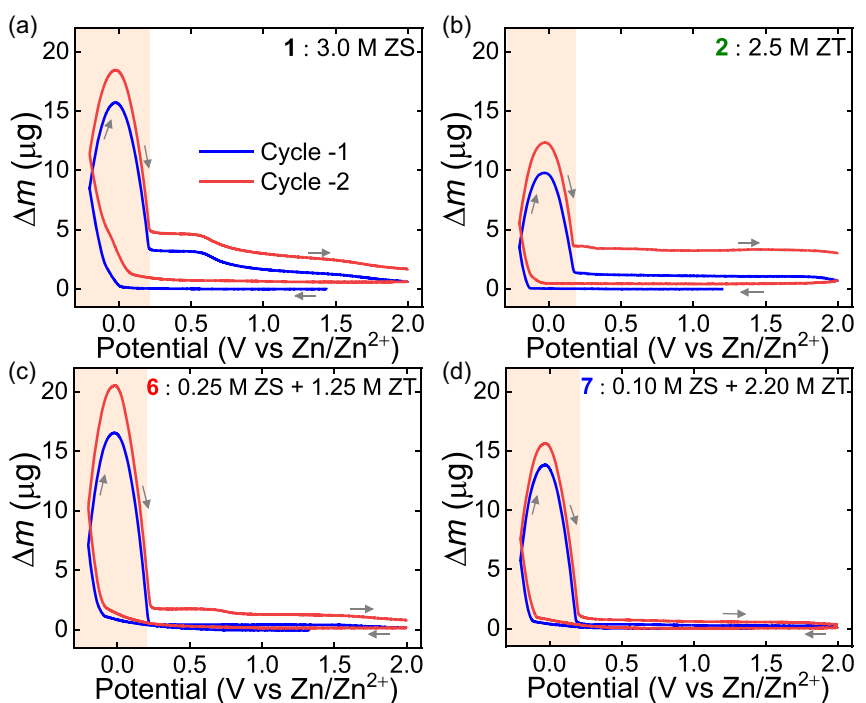


Figure 4. Comparative mass analysis of zinc deposition and dissolution during two consecutive cycles at the same scan rate ($v = 10 \text{ mV s}^{-1}$) in electrochemical cycling for electrolytes a) 1, b) 2, c) 6, and d) 7.

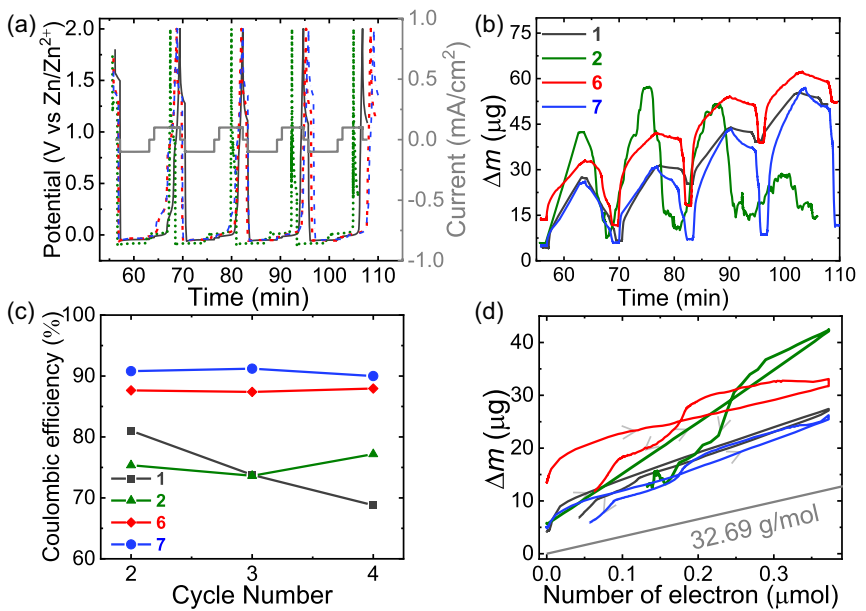


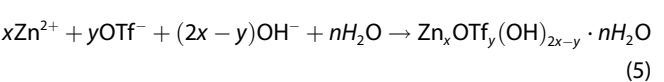
Figure 5. GCPL cycling performance of various electrolytes (1, 2, 6, and 7): a) galvanostatic voltage profile, b) comparative mass analysis for different galvanostatic cycles, c) CE in different cycles, d) mass per electron profile of the first galvanostatic cycle.

increase, indicating efficient Zn dissolution without a major irreversible passivation effect. This behavior points to the development of a homogeneous and compact Zn layer that dissolves gradually and requires less surplus energy to strip completely.

From the mass change analysis during GCPL cycling (Figure 5b), we observed a progressive increase in mass irreversibility in 3.0 M ZS, indicative of persistent byproduct accumulation mainly due to continuous parasitic reactions such as HER, which remain unmitigated due to the absence of a protective interphase layer, and is further corroborated by the gradual decline in CE over cycling (Figure 5c). In 2.5 M ZT, mass reversibility remained high; however, the total mass deposition amount dropped dramatically, which may affect battery capacity.^[59] This behavior suggests the formation of a rigid interfacial layer, which minimizes side reactions by restricting direct electrode–electrolyte interaction but progressively impedes Zn²⁺ diffusion through the layer over prolonged cycling. On the contrary, hybrid electrolytes, especially 0.10 M ZS + 2.20 M ZT, showed better reversibility than pure ones, aligned with the voltammetric results. The enhanced Zn²⁺ diffusion combined with reduced irreversibility suggests the formation of an ion-conductive passivation layer that selectively facilitates Zn²⁺ transport while suppressing the migration of other species responsible for side reactions. Such a layer is expected to promote efficient Zn exchange, thereby ensuring long-term cycling stability and improved battery performance. This interpretation is further supported by the highest and most stable CE (Figure 5c) and the near-ideal mpe curve (Figure 5d) observed for the hybrid electrolyte, indicating improved Zn plating/stripping efficiency and reduced side reactions.

Figure 6 showcased the structural and morphological analyses of the electrode surfaces to elucidate the formation of irreversible byproducts in different electrolytes, as inferred from the previous mass change analysis. The distinct XRD peak at a

two-theta value of 8.4° in Figure 6a is characteristic of the namuwite-type ZHS byproduct formed in the pure zinc sulfate electrolyte.^[60] In contrast, the pure triflate electrolyte exhibits a weak reflection near 2θ = 18°, which is commonly attributed to the formation of a Zn(OH)₂ surface layer. However, recent studies have also associated this peak with the formation of an irreversible byproduct layer ZOTH, particularly in triflate-based systems.^[61,62] The formation of these byproducts follows a similar mechanism, wherein OH⁻ ions generated during the HER react with Zn²⁺ ions, the corresponding anions (SO₄²⁻ and CF₃SO₃⁻), and free water molecules, as illustrated by the following equations.^[33,63-65]



Here, the hydration number (*n*) is primarily influenced by the local pH and concentration of electrolytes. Both ZHS and ZOTH peaks were observed in the hybrid electrolytes, especially in electrolytes 5, 6, and 7, indicating a hybrid surface composition caused by the coexistence of sulfate and triflate anions, which is consistent with the distinct surface characteristics of forming an ion-conductive passivation layer discussed before. The slight rightward shift in Figure 6a of the ZHS peak (2θ = 8.4°) in

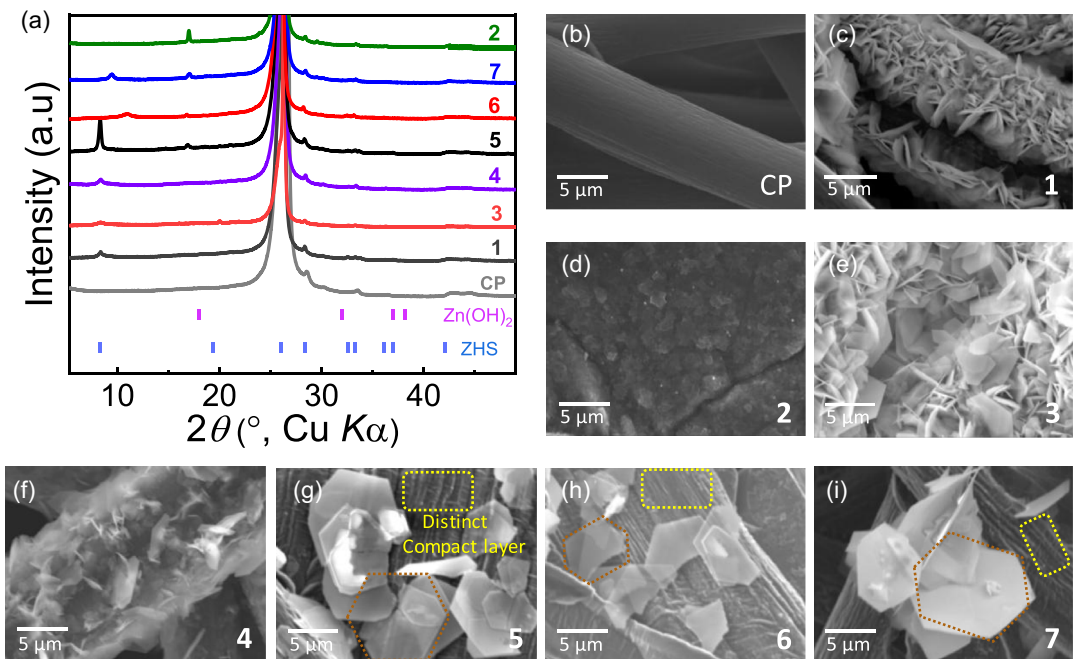


Figure 6. Morphological characterization of surface film on the carbon paper as WEs in the presence of different electrolytes. a) XRD pattern of carbon electrode by utilizing various electrolytes; and b–i) SEM images of bare carbon electrode and carbon electrodes after cycling with different electrolytes.

electrolytes **6** and **7** is attributed to a decrease in the hydration number (n) within the ZHS composition, indicating suppressed water activity in these electrolytes.^[66,67]

Following cycling in the 3.0 M ZS electrolyte, the SEM picture displayed in Figure 6c shows the development of a porous surface morphology with loosely bonded hexagonal sheet-like structures on the carbon electrode, signifying the formation of ZHS byproducts, further supported by the presence of Zn, S, and O from EDS mapping (Figure S10a, Supporting Information). The ZHS sheets observed on the carbon electrodes exhibited dimensions ranging from ≈ 3 – 10 μm. The formation of a uniform and rigid surface layer over the electrode surface, observed in the case of the pure triflate electrolyte (Figure 6d), is well aligned with the low ΔR_m

recorded by EQCM. The rigid layer enhances reversibility but also hinders Zn^{2+} diffusion, as discussed in the GCPL analysis. EDS mapping confirmed the presence of Zn, O, S, and F elements (Figure S10b, Supporting Information), suggesting that the surface film may consist of $\text{Zn}(\text{OH})_2$, ZnO , and ZOTH. Hybrid electrolytes (Figure 6h,i) showed suppressed byproduct formation and the development of a distinct compact layer compared to pure electrolytes, which likely contributes to improved electrochemical performance, high mass reversibility, and near-to-ideal mpe values.

Atomic force microscopy (AFM) analysis was carried out to assess the surface morphology of electrode surfaces after cycling in different electrolytes (Figure 7). The highest roughness, characterized by the root mean square of the surface height for the

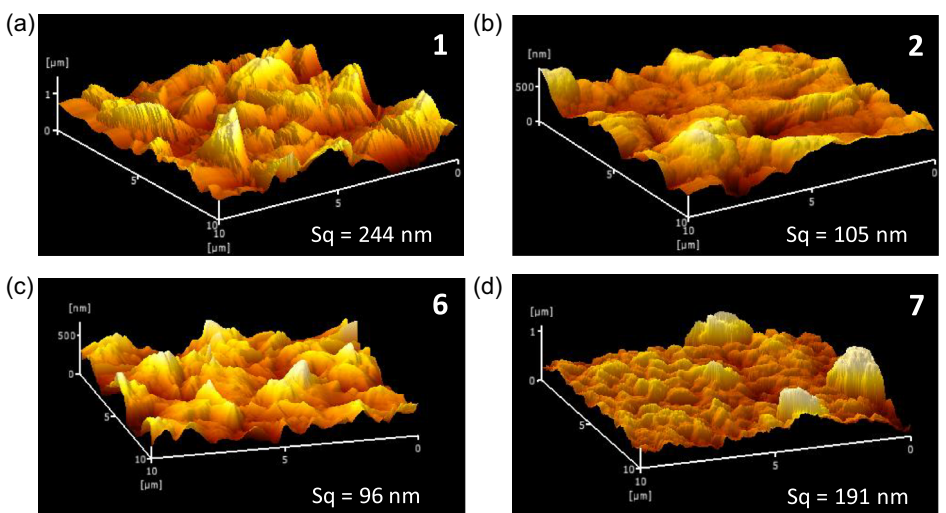


Figure 7. AFM images of cycled stainless steel electrodes in various electrolytes: a) 1, b) 2, c) 6, and d) 7.

selected area (S_q) value of 244 nm, was observed for 3.0 M ZS, indicating a nonuniform interphase likely caused by extensive side reactions. In contrast, 2.5 M ZT showed a smoother, more compact layer ($S_q = 105$ nm), as illustrated in the schematic diagram. Notably, the hybrid electrolyte 6 exhibited the lowest roughness ($S_q = 96$ nm), suggesting a uniform interfacial layer enabled by dual-anion coordination, while electrolyte 7 showed moderate roughness ($S_q = 191$ nm), likely due to the presence of localized protrusions or humps. More uniform deposition in electrolytes 2 and 6 might be related to the higher interfacial charge transfer impedance (Figure 8), which leads to more uniform secondary current distribution.

The Nyquist plot obtained from electrochemical impedance spectroscopy (EIS) analysis at open-circuit voltage (OCV) (Figure 8a) sheds light on significant differences in interfacial behavior on the Zn surface across the various electrolytes. Electrolytes 2 and 6 exhibited larger semicircle diameters in the Nyquist plots, indicating higher charge transfer resistance (R_{ct}), which may be attributed to the formation of a protective surface layer. This protective layer is likely responsible for the enhanced cycling stability observed in the $Zn||Zn$ symmetric cell tests, as discussed in the following section. In contrast, electrolytes 1 and 7 displayed semi-infinite diffusion behavior with smaller R_{ct} , suggesting the absence of significant surface film formation on the electrode surface.

To clearly distinguish the individual electrochemical processes based on their respective relaxation times (τ), which is challenging using EIS alone due to overlapping semicircles, distribution of relaxation time (DRT) analysis was performed (Figure 8b). A broader peak in the lower τ region depicts the porous nature of the electrode-electrolyte interface (R_{ZHS}), which facilitates easier ion transport.^[68] However, a single sharp peak around 10^{-2} s corresponds to the slower charge transfer kinetics attributed to the rigid layer formation by pure triflate electrolyte, as discussed earlier. Interestingly, in a 0.25 M ZS + 1.25 M ZT electrolyte, two highly prominent peaks were observed. The peak at lower τ values corresponds to the porous interfacial behavior, while the shoulder peak at higher τ values is associated with the formation of a protective surface layer (R_{SEI}). This DRT analysis further confirms the distinct electrode-electrolyte interfacial characteristics achieved with the hybrid electrolyte compared to the pure system, which can enhance the electrochemical performance.

Attenuated total reflection Fourier-transform infrared (ATR-FTIR) spectroscopy was performed to probe the surface composition of cycled electrodes (Figure 9). The broad O-H stretching band (3200 – 3600 cm^{-1}) shifted to lower wavenumbers in hybrid electrolytes (6 and 7), indicating stronger H-bonding in the solvation shell and reduced water activity, thus supporting HER suppression.^[69] Additionally, a distinct shoulder in this region was

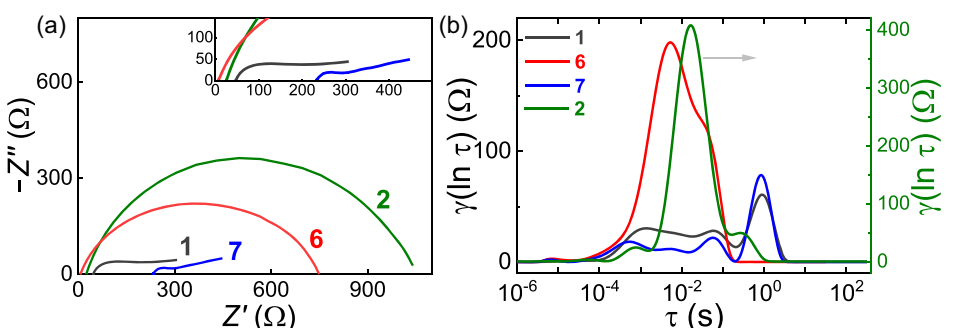


Figure 8. Electrochemical characterization of the system: a) EIS nyquist plot at OCV, illustrating impedance behavior and charge transfer resistance, and b) DRT analysis to elucidate the contributions of various electrochemical processes within the system.

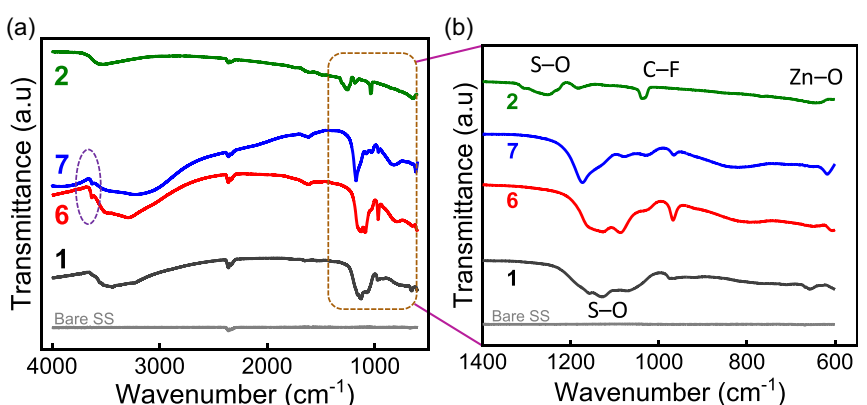


Figure 9. ATR-FTIR spectra of cycled stainless steel electrodes after cycling in different electrolytes 1, 2, 6, and 7: a) full spectral range and b) enlarged view of the 1400 – 600 cm^{-1} fingerprint region highlighting Zn–O, S–O, and C–F vibrational modes.

observed exclusively in the hybrid systems, suggesting the presence of a unique hydrogen-bonding environment likely arising from dual-anion coordination around Zn^{2+} . In the fingerprint region (Figure 9b), characteristic peaks for S–O ($\approx 1100\text{ cm}^{-1}$), C–F ($\approx 1038\text{ cm}^{-1}$), and Zn–O ($\approx 600\text{ cm}^{-1}$) were observed. A slight red shift in the characteristic vibrational peaks was observed for the mixed electrolytes, indicating a modified coordination environment due to the dual-anion effect. This shift suggests increased Zn^{2+} -anion separation and the formation of a more structured solvation shell, which enhances water binding and reduces water reactivity, thereby suppressing HER.^[70,71] These findings support the formation of a compositionally regulated interfacial layer in hybrid electrolytes, consistent with EQCM data. X-ray photoelectron spectroscopy (XPS) characterization was conducted to further investigate interfacial chemistry and byproduct formation (Figure S11, Supporting Information). In pure ZS electrolyte, shoulder features in Zn 2p (1024eV) and O 1s (535 eV) spectra indicate $Zn(OH)_2$ and ZHS formation.^[46,65] These signals are significantly suppressed in hybrid electrolytes, suggesting reduced parasitic reactions. Conversely, strong CF_3^- -related peaks in the F 1s and C 1s spectra of ZT imply the presence of triflate-derived byproducts (e.g., ZOTH), which diminish in hybrid systems, indicating moderated passivation layer formation.^[33,72] These results corroborate the dual-anion coordination mechanism proposed from FTIR and EQCM data.

The $Zn||Zn$ symmetric cell configuration offers critical insights into long-term interfacial stability and dendrite suppression under excess Zn conditions, effectively simulating conventional

Zn metal anode-based batteries (Figure 10). The cell with 3.0 M ZS electrolyte exhibited a limited cycle life of ≈ 100 h, primarily due to the formation of byproducts such as (ZHS) and severe dendritic growth, resulting from nonuniform Zn deposition.^[73] In contrast, the cell using 2.5 M ZT demonstrated significantly extended stability, achieving a cycle life of up to 800 h without short-circuiting. This enhancement can be attributed to forming a rigid interfacial layer, which may effectively suppress dendrite growth and parasitic reactions by minimizing water activity.^[74] Despite reduced Zn plating/stripping observed during GCPL analysis, the excess Zn available in this symmetric configuration likely compensated for the limited active mass cycling, thereby preserving cell longevity. Among the hybrid electrolytes, the 0.25 M ZS + 1.25 M ZT system delivered an intermediate yet promising cycle life of ≈ 650 h, while the 0.10 M ZS + 2.20 M ZT electrolyte showed a surprisingly short lifetime of 50 h, which may be due to the presence of localized protrusions or humps as shown in AFM images.

The $Cu||Zn$ asymmetric cell serves as an analog for anode-free Zn -ion battery configurations and is particularly suited to evaluating the reversibility of Zn deposition on a bare current collector (Figure 11). Unlike symmetric cells, where dendrite formation often leads to short-circuiting, the Cu-based configuration highlights plating/stripping reversibility via CE value. The 3.0 M ZS electrolyte delivered exceptional stability, with the cell cycling for over 2,000 h without failure, likely due to the formation of a partially dissolvable ZHS layer that facilitates reversible Zn deposition on the Cu substrate while avoiding the short-circuit due to the insulating nature of ZHS. Conversely, the 2.5 M ZT

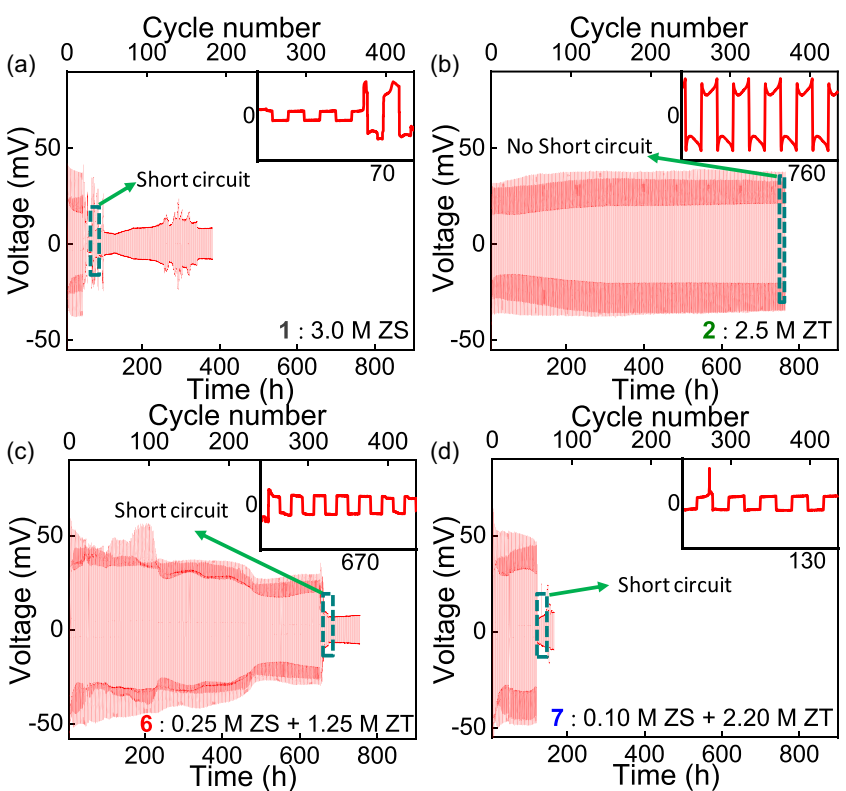


Figure 10. Long-term cycling of $Zn||Zn$ symmetric cells by using electrolytes a) 1, b) 2, c) 6, and d) 7.

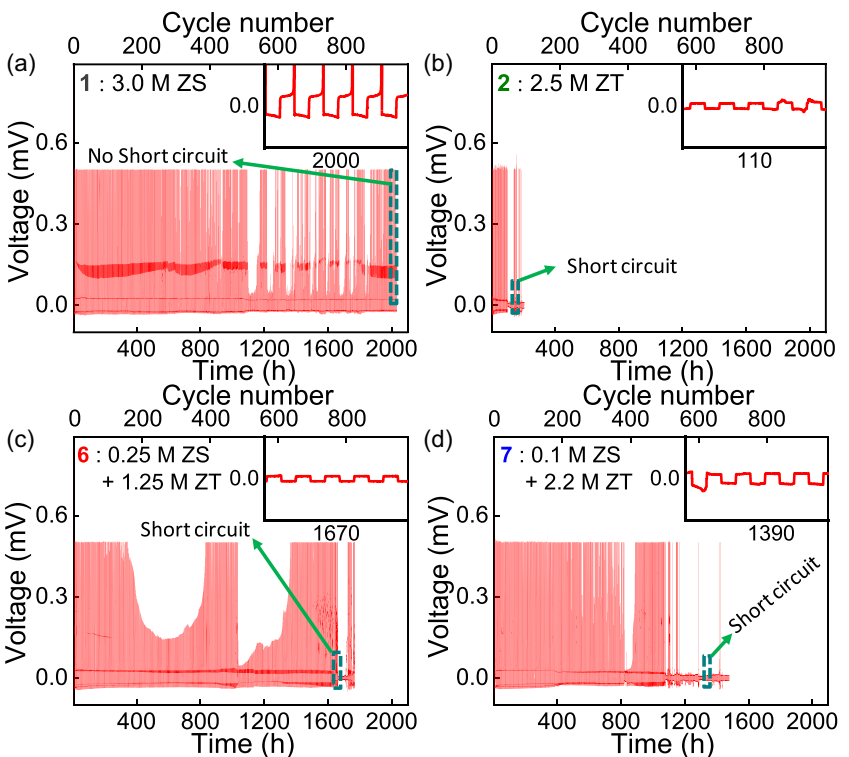


Figure 11. Electrochemical performance of Cu||Zn asymmetric cells using electrolytes a) 1, b) 2, c) 6, and d) 7.

electrolyte, despite suppressing dendrites in the symmetric cell, suffered from poor reversibility and reduced Zn deposition, likely due to the formation of a dense, rigid interphase. This led to a markedly shorter cycle life of ≈ 100 h, as reflected by the lower CE.^[75] Notably, the hybrid electrolyte 0.25 M ZS + 1.25 M ZT achieved extended cycling stability of ≈ 1750 h, and the 0.10 M ZS + 2.20 M ZT also performed well till 1380 h, reflecting a synergistic interfacial modulation that balanced rigidity for parasitic reaction suppression with porosity for efficient Zn^{2+} transport. The enhanced stability of the hybrid electrolytes highlights the synergistic effect of sulfate and triflate anions in promoting uniform Zn deposition and suppressing side reactions, critical for achieving high reversibility and extended cycling performance.

Together, the results from both Zn||Zn and Cu||Zn configurations demonstrate that the 0.25 M ZS + 1.25 M ZT DSHE offers the most balanced performance. It exhibits excellent long-term cycling stability, efficient Zn plating/stripping behavior, and minimized interfacial degradation, attributed to the cooperative role of sulfate and triflate anions in stabilizing the electrode-electrolyte interface. With further optimization, this electrolyte system holds strong potential for enabling high-performance, durable aqueous Zn-based batteries for future grid and consumer energy storage applications.

3. Conclusion

In summary, we have demonstrated the application of the EQCM technique to investigate the interfacial behavior and passivation

characteristics of Zn metal anodes in sulfate electrolyte, triflate electrolyte, and DSHEs. The viscoelastic surface layer formed in the case of 3.0 M ZS, though facilitating Zn^{2+} leads to nonuniform Zn deposition along with pronounced side reactions such as HER and ZHS formation. Conversely, 2.5 M ZT was able to suppress side reactions through rigid interphase formation yet hindered Zn^{2+} transport. Notably, the DSHE demonstrated a balanced interfacial structure that was mechanically robust to suppress parasitic side reactions, while retaining adequate ionic mobility to enable efficient Zn^{2+} transport. These synergistic interfacial effects led to improved mass reversibility and near-to-ideal mpe values. Other characterizations, like conductivity, XRD, SEM-EDS, EIS, AFM, and ATR-FTIR, suggested the superiority of DSHEs. This work provides fundamental insights into protective layer formation by different electrolytes and highlights the potential of dual-salt electrolyte engineering as a strategy to advance high-performance AZBs.

4. Experimental Section

Electrolyte Preparation

In this study, seven distinct electrolyte formulations were systematically prepared by dissolving stoichiometric amounts of Zn salts—zinc sulfate heptahydrate ($ZnSO_4 \cdot 7H_2O$; ZS; 99%; Daejung Co.) and zinc trifluoromethanesulfonate ($Zn(OTf)_2$; ZT; 98%; Sigma-Aldrich), in doubly deionized water. The solutions were stirred at room temperature for 24 h to ensure complete dissolution. The specific electrolyte compositions (designated as electrolytes 1–7) utilized in this

investigation were outlined as follows: 3.0 M ZS (1), 2.5 M ZT (2), 1.50 M ZS + 0.05 M ZT (3), 1.25 M ZS + 0.25 M ZT (4), 0.75 M ZS + 0.75 M ZT (5), 0.25 M ZS + 1.25 M ZT (6), 0.10 M ZS + 2.20 M ZT (7). Electrolytes 1 and 2 served as literature-reported baselines. Mixed electrolytes (3–6) were designed to maintain a comparable total Zn^{2+} concentration (≈ 1.5 M), which falls within the optimal conductivity range (1.5–2.0 M) identified in our previous conductivity studies,^[66] while gradually increasing ZT content to investigate the impact of triflate anion incorporation, known to suppress hydrogen evolution and improve interfacial stability. Electrolyte 7 was prepared near the solubility limit to achieve maximum ZT concentration with minimal ZS, enabling exploration of the triflate-dominant regime.

Electrochemical and EQCM Measurement

All electrochemical measurements were performed using a three-electrode configuration under room temperature and ambient air conditions using a VMP3 potentiostat (Bio-Logic Co.) controlled through EC-Lab software. For EQCM analysis, the potentiostat was integrated with a QCA922 (Seiko EG&G Co.) instrument, and measurements were carried out using a custom-built airtight EQCM cell. The working electrode (WE) employed was an AT-cut quartz crystal (Neoscience Co.) with a platinum-coated working area of 0.196 cm^2 , a sensitivity factor (C_f) of around $926.80\text{ Hz mg}^{-1}\text{ cm}^2$, and a resonance frequency of 8.99 MHz. Zn foils (99.98%; Alfa Aesar Co.) with a thickness of 0.25 mm were spot-welded on a stainless-steel foil serving as the current collector. These foils were utilized as reference electrode (RE) and counter electrodes (CE), with dimensions of $0.3 \times 1\text{ cm}$ and $1 \times 1\text{ cm}$, respectively, for electrochemical measurements and other surface characterization. During EQCM measurements, mass changes associated with zinc deposition and dissolution in various electrolytes were monitored by performing multiple CV cycles within a potential range of -0.2 V to 2.0 V versus Zn/Zn^{2+} , followed by successive galvanostatic charge-discharge cycles.

ESW was evaluated by CV using a platinum wire as the WE and Zn foil as both RE and CE. The scan was performed from 0.5 V to 2.5 V versus Zn/Zn^{2+} . The Zn^{2+} transference number (t_+) was determined using the Bruce–Vincent method. Symmetric $Zn||Zn$ cells were assembled for this purpose, and the calculation was based on chronoamperometry combined with EIS measurements obtained before and after polarization. pH measurements of the electrolytes were conducted before and after electrochemical cycling using a digital pH meter (Lab 845, SI Analytics Co.) to quantify HER activity. During EIS measurements, a Zn foil with dimensions $1 \times 1\text{ cm}$ was used as the WE to analyze the impedance response of different electrolytes within the electrochemical system.

Surface Characterization

To investigate the structural and interfacial evolution during zinc deposition/dissolution, surface characterizations were conducted after several cycles of CV and galvanostatic plating/stripping in various electrolytes. Carbon paper ($1 \times 1\text{ cm}$, MGL 190 μm , AvCarb Co.) and stainless-steel foil ($1 \times 1\text{ cm}$) were used as WEs for postmortem analysis. After cycling, the electrodes were thoroughly rinsed with deionized water to remove residual Zn salts and vacuum-dried for 1 h.

XRD analysis was employed using a Miniflex600 diffractometer (Rigaku Co.) with $Cu K\alpha$ radiation to investigate the phase structure. SEM-EDS (JSM-IT210; JEOL Ltd.) was used for morphological and compositional analysis of the surface film formed over the carbon substrate. To gain further insights into interfacial layer composition and topography, AFM(AFM5100N, HITACHI, Japan),

ATR-FTIR(NICOLET iS20, Thermo Fischer Scientific), and XPS(AXIS SUPRA, Kratos Analytical Co.) were performed using stainless steel substrates.

Conductivity Measurement

The ionic conductivity of the different electrolyte solutions was measured using a digital conductometer (Lab 955, SI Analytics Co.) equipped with a conductivity probe (Cell constant: 0.850 cm^{-1}). Prior to measurement, the conductometer was calibrated using standard 0.01 M KCl solutions. All measurements were performed at 25°C under ambient conditions. The instrument automatically determined the conductivity and expressed it in mS cm^{-1} .

Electrochemical Stability Test

To assess the long-term cycling stability of the Zn plating/stripping process in different electrolytes, $Zn||Zn$ symmetric and $Cu||Zn$ asymmetric cells were assembled using CR2032-type coin cells. Electrochemical cycling was conducted using a WBCS3000L (WonaAtech) automatic battery cycler under controlled conditions. Glass fiber prefilters (1.6 μm pore size; Merk Millipore Ltd.) were used as the separator in the assembled cells. All electrodes used in this test were punched using a 14 mm diameter punching tool, resulting in a geometric surface area of 1.54 cm^2 , and subsequently pressed and lightly scratched to enhance the active Zn surface area. For $Zn||Zn$ symmetric cells, both electrodes were composed of 0.25 mm thick Zn foils. The cells were subjected to galvanostatic charge-discharge cycling at an areal capacity of 1 mA cm^2 with a time duration of one hour per cycle. For $Zn||Cu$ asymmetric cells, a Cu foil with a thickness of 0.12 mm was used as the WE. The charge-discharge cycling was performed under the same conditions as $Zn||Zn$ symmetric cells (1 mAh cm^{-2}) with an additional charging cutoff voltage of 0.5 V vs. Zn/Zn^{2+} to prevent copper dissolution. Before initiating the cycling tests, an initial resting period of 6 hr was applied with an additional one-minute resting interval between each cycle to all coin cells.

Acknowledgements

This research was supported by the Basic Science Research Program through the National Research Foundation of Korea (NRF), funded by the Ministry of Science and ICT (grant nos. NRF-2021R1C1C1005446, RS-2025-00512708). This research was also supported by Korea Electric Power Corporation (grant no. R22XO02-04) and Global-Learning & Academic research institution for Master's-PhD students and Postdocs (G-LAMP) Program of the NRF grant funded by the Ministry of Education (grant no. RS-2023-00301938).

Conflict of Interest

The authors declare no conflict of interest.

Data Availability Statement

The data that support the findings of this study are available from the corresponding author upon reasonable request.

Keywords: aqueous zinc-ion battery · dual-salt hybrid electrolyte · electrochemical quartz-crystal microbalance · motional resistance · passivation layer

- [1] H. Kim, G. Jeong, Y.-U. Kim, J.-H. Kim, C.-M. Park, H.-J. Sohn, *Chem. Soc. Rev.* **2013**, *42*, 9011.
- [2] F. Du, F. Wu, L. Ma, J. Feng, X. Yin, Y. Wang, X. Dai, W. Liu, W. Shi, X. Cao, *Funct. Mater. Lett.* **2023**, *16*, 2340017.
- [3] X. Li, J. Zeng, H. Yao, D. Yuan, L. Zhang, *ChemNanoMat.* **2021**, *7*, 1162.
- [4] H. Li, Z. Wang, L. Chen, X. Huang, *Adv. Mater.* **2009**, *21*, 4593.
- [5] D. Deng, *Energy Sci. Eng.* **2015**, *3*, 385.
- [6] M. S. Whittingham, *Chem. Rev.* **2004**, *104*, 4271.
- [7] D. Zhang, J. Cao, C. Yang, K. Lolupiman, W. Limphirat, X. Wu, X. Zhang, J. Qin, Y. Huang, *Adv. Energy Mater.* **2025**, *15*, 2404026.
- [8] L. Kou, Y. Wang, J. Song, T. Ai, W. Li, P. Wattanapaphawong, K. Kajiyoshi, M. Y. Ghobbi, Y. Feng, *Inorg. Chem. Front.* **2024**, *11*, 1949.
- [9] C. Nie, G. Wang, D. Wang, M. Wang, X. Gao, Z. Bai, N. Wang, J. Yang, Z. Xing, S. Dou, *Adv. Energy Mater.* **2023**, *13*, 2300606.
- [10] Y. Xu, G. Zhang, J. Liu, J. Zhang, X. Wang, X. Pu, J. Wang, C. Yan, Y. Cao, H. Yang, W. Li, X. Li, *Energy Environ. Mater.* **2023**, *6*, e12575.
- [11] J. Cao, H. Wu, Y. Yue, D. Zhang, B. Li, D. Luo, L. Zhang, J. Qin, X. Zhang, X. Yang, *J. Energy Chem.* **2024**, *99*, 671.
- [12] L. Kang, M. Cui, Z. Zhang, F. Jiang, *Batteries Supercaps.* **2020**, *3*, 966.
- [13] Z. Xiong, W. Jin, H. Liu, H. Liu, *Adv. Energy Sustainability Res.* **2022**, *3*, 2100194.
- [14] B. Yong, D. Ma, Y. Wang, H. Mi, C. He, P. Zhang, *Adv. Energy Mater.* **2020**, *10*, 2002354.
- [15] X. Zhang, C. Jia, J. Zhang, L. Zhang, X. Liu, *Adv. Sci.* **2024**, *11*, 2305201.
- [16] Y. Liu, H. Wang, Q. Li, L. Zhou, P. Zhao, R. Holze, *Energies* **2023**, *16*, 7443.
- [17] J. Cao, X. Wang, S. Qian, D. Zhang, D. Luo, L. Zhang, J. Qin, X. Zhang, X. Yang, J. Lu, *Adv. Mater.* **2024**, *36*, 2410947.
- [18] H. Du, Z. Yi, H. Li, W. Lv, N. Hu, X. Zhang, W. Chen, Z. Wei, F. Shen, H. He, *Chem. Eur. J.* **2024**, *30*, e202303461.
- [19] J. Chen, M. Chen, H. Ma, W. Zhou, X. Xu, *Energy Rev.* **2022**, *1*, 100005.
- [20] J. Cao, Z. Yuan, C. Li, F. Zhao, Q. Zhao, L. Gao, T. Ma, X. Ren, X. Li, A. Liu, *J. Mater. Chem. A.* **2024**, *12*, 29869.
- [21] G. Li, L. Sun, S. Zhang, C. Zhang, H. Jin, K. Davey, G. Liang, S. Liu, J. Mao, Z. Guo, *Adv. Funct. Mater.* **2024**, *34*, 2301291.
- [22] Y. Tang, J. H. Li, C. L. Xu, M. Liu, B. Xiao, P. F. Wang, *Carbon Neutraliz.* **2023**, *2*, 186.
- [23] D. Zhang, Y. Yue, C. Yang, W. Limphirat, X. Zhang, J. Qin, J. Cao, *Chem. Eng. J.* **2025**, *506*, 160160.
- [24] J. Wei, P. Zhang, J. Sun, Y. Liu, F. Li, H. Xu, R. Ye, Z. Tie, L. Sun, Z. Jin, *Chem. Soc. Rev.* **2024**, *53*, 10335.
- [25] Y. Liang, M. Qiu, P. Sun, W. Mai, *Adv. Funct. Mater.* **2023**, *33*, 2304878.
- [26] Y. Geng, L. Pan, Z. Peng, Z. Sun, H. Lin, C. Mao, L. Wang, L. Dai, H. Liu, K. Pan, X. Wu, Q. Zhang, Z. He, *Energy Storage Mater.* **2022**, *51*, 733.
- [27] N. Zhang, F. Cheng, J. Liu, L. Wang, X. Long, X. Liu, F. Li, J. Chen, *Nat. Commun.* **2017**, *8*, 405.
- [28] T. Yamamoto, T. Shoji *Inorg. Chim. Acta.* **1986**, *117*, L27.
- [29] J. Zhu, Z. Tie, S. Bi, Z. Niu *Angew. Chem., Int. Ed.* **2024**, *63*, e202403712.
- [30] Q. Zhang, Z. Yang, H. Ji, X. Zeng, Y. Tang, D. Sun, H. Wang, *SusMat* **2021**, *1*, 432.
- [31] W. Zhuoxi, H. Zhaodong, Z. Rong, H. Yue, Z. Chunyi, *Int. J. Extrem. Manuf.* **2024**, *6*, 062002.
- [32] R. Rajabi, S. Sun, A. Billings, V. F. Mattick, J. Khan, K. Huang, *J. Electrochem. Soc.* **2022**, *169*, 110536.
- [33] H. Zhao, M. Wan, X. Zhu, X. Cui, X. Du, R. Zheng, H. Zhong, H. Wang, *ACS Applied Nano Mater.* **2024**, *7*, 23712.
- [34] N. A. Thieu, W. Li, X. Chen, Q. Li, Q. Wang, M. Velayutham, Z. M. Grady, X. Li, W. Li, V. V. Khrantsov, D. M. Reed, X. Li, X. Liu, *ACS Appl. Mater. Interfaces* **2023**, *15*, 55570.
- [35] X. Guo, G. He, *J. Mater. Chem. A.* **2023**, *11*, 11987.
- [36] B. Zhang, J. Yao, C. Wu, Y. Li, J. Liu, J. Wang, T. Xiao, T. Zhang, D. Cai, J. Wu, Z. W. Seh, S. Xi, H. Wang, W. Sun, H. Wan, H. J. Fan, *Nat. Commun.* **2025**, *16*, 71.
- [37] S. Liu, R. Zhang, J. Mao, Y. Zhao, Q. Cai, Z. Guo, *Sci. Adv.* **2022**, *8*, eabn5097.
- [38] T. Fang, M. Wu, F. Lu, Z. Zhou, Y. Fu, Z. Shi, *Energy Mater.* **2024**, *4*, 400039.
- [39] K. Feng, Y. Zhao, Z. Liu, Y. Yu, *J. Colloid Interface Sci.* **2025**, *678*, 76.
- [40] A. O. Efremova, A. I. Volkov, E. G. Tolstopyatova, V. V. Kondratiev, *J. Alloys Compd.* **2022**, *892*, 162142.
- [41] G. Sauerbrey, *Z. Phys.* **1959**, *155*, 206.
- [42] T. Nomura, M. Okuhara, *Anal. Chim. Acta.* **1982**, *142*, 281.
- [43] X. Huang, Q. Bai, Q. Zhou, J. Hu, *Sensors* **2017**, *17*, 1476.
- [44] J. Barthel, H. Hetzenauer, R. Buchner, *Ber. Bunsenges. Phys. Chem.* **1992**, *96*, 1424.
- [45] J. Hao, X. Li, S. Zhang, F. Yang, X. Zeng, S. Zhang, G. Bo, C. Wang, Z. Guo, *Adv. Funct. Mater.* **2020**, *30*, 2001263.
- [46] W. Zhang, M. Dong, K. Jiang, D. Yang, X. Tan, S. Zhai, R. Feng, N. Chen, G. King, H. Zhang, H. Zeng, H. Li, M. Antonietti, Z. Li, *Nat. Commun.* **2022**, *13*, 5348.
- [47] Z. Wu, J. Liu, *Batteries Supercaps* **2024**, *7*, e202400483.
- [48] W. Sun, F. Wang, B. Zhang, M. Zhang, V. Küpers, X. Ji, C. Theile, P. Bieker, K. Xu, C. Wang, M. Winter, *Sciences* **2021**, *371*, 46.
- [49] C. Likitaporn, M. Okhawilai, N. Senthilkumar, T. Wongsalam, N. Tanalue, P. Kasemsiri, J. Qin, H. Uyama, *Sci. Rep.* **2023**, *13*, 16774.
- [50] Z. Ye, Z. Cao, M. O. L. Chee, P. Dong, P. M. Ajayan, J. Shen, M. Ye, *Energy Storage Mater.* **2020**, *32*, 290.
- [51] G. Zhang, J. Chang, L. Wang, J. Li, C. Wang, R. Wang, G. Shi, K. Yu, W. Huang, H. Zheng, T. Wu, Y. Deng, J. Lu, *Nat. Commun.* **2023**, *14*, 1081.
- [52] Y. Zhao, T. Zhou, M. Mensi, J. W. Choi, A. Coskun, *Nat. Commun.* **2023**, *14*, 299.
- [53] J. Evans, C. A. Vincent, P. G. Bruce, *Polymer* **1987**, *28*, 2324.
- [54] J. Weng, W. Zhu, K. Yu, J. Luo, M. Chen, L. Li, Y. Zhuang, K. Xia, Z. Lu, Y. Hu, C. Yang, M. Wu, Z. Zou, *Adv. Funct. Mater.* **2024**, *34*, 2314347.
- [55] J. H. Jo, Y. Aniskevich, J. Kim, J. U. Choi, H. J. Kim, Y. H. Jung, D. Ahn, T. Y. Jeon, K. S. Lee, S. H. Song, H. Kim, G. Ragoisha, A. Mazanik, E. Streltsov, S. T. Myung, *Adv. Energy Mater.* **2020**, *10*, 2010595.
- [56] N. Zhang, F. Cheng, Y. Liu, Q. Zhao, K. Lei, C. Chen, X. Liu, J. Chen, *J. Am. Chem. Soc.* **2016**, *138*, 12894.
- [57] J. Agrisuelas, C. Gabrielli, J. J. García-Jareño, H. Perrot, O. Sel, F. Vicente, *Electrochim. Acta* **2015**, *176*, 1454.
- [58] X. Zhou, Y. Lu, Q. Zhang, L. Miao, K. Zhang, Z. Yan, F. Li, J. Chen, *ACS Appl. Mater. Interfaces* **2020**, *12*, 55476.
- [59] L. Luo, Z. Wen, G. Hong, S. Chen, *RSC Adv.* **2023**, *13*, 34947.
- [60] Y. Wang, X. Liao, W. Wang, S. Chen, J. Chen, H. Wang, *ACS Appl. Mater. Interfaces* **2024**, *16*, 14912.
- [61] B. Niu, Z. Li, D. Luo, X. Ma, Q. Yang, Y.-E. Liu, X. Yu, X. He, Y. Qiao, X. Wang, *Energy Environ. Sci.* **2023**, *16*, 1662.
- [62] L. Wang, K.-W. Huang, J. Chen, J. Zheng, *Sci. Adv.* **2019**, *5*, eaax4279.
- [63] X. Zhao, N. Dong, M. Yan, H. Pan, *ACS Appl. Mater. Interfaces* **2023**, *15*, 4053.
- [64] W. G. Lim, X. Li, D. Reed, *Small Methods* **2024**, *8*, 2300965.
- [65] L. Godeffroy, I. Aguilar, J. Médard, D. Larcher, J. M. Tarascon, F. Kanoufi, *Adv. Energy Mater.* **2022**, *12*, 2200722.
- [66] S. K. Mohanty, Y. Ok, E. S. Kim, Y. Park, J. H. Ryu, J. Mun, J. Lee, K. Hyun, M. K. Srinivasa, H. Jeong, S. C. Reddy, H. D. Yoo, *Batteries Supercaps* **2024**, *7*, e202400338.
- [67] I. J. Bear, I. E. Grey, I. C. Madsen, I. E. Newnham, L. J. Rogers, *Acta Crystallogr. B Struct. Sci.* **1986**, *42*, 32.
- [68] S. Wang, Y. Zhao, H. Lv, X. Hu, J. He, C. Zhi, H. Li, *Small* **2024**, *20*, 2207664.
- [69] M. Lounasvuori, T. S. Mathis, Y. Gogotsi, T. Petit, *J. Phys. Chem. Lett.* **2023**, *14*, 1578.
- [70] T. A. Nigatu, H. K. Bezabih, B. W. Taklu, B. W. Olbasa, Y.-T. Weng, S.-H. Wu, W.-N. Su, C.-C. Yang, B. J. Hwang, *J. Power Sources* **2021**, *511*, 230413.
- [71] S. C. Myneni, *Rev. Mineral. Geochem.* **2000**, *40*, 113.
- [72] S. Di, X. Nie, G. Ma, W. Yuan, Y. Wang, Y. Liu, S. Shen, N. Zhang, *Energy Storage Mater.* **2021**, *43*, 375.
- [73] K. Zhao, F. Liu, G. Fan, J. Liu, M. Yu, Z. Yan, N. Zhang, F. Cheng, *ACS Appl. Mater. Interfaces* **2021**, *13*, 47650.
- [74] N. Zhang, F. Cheng, Y. Liu, Q. Zhao, K. Lei, C. Chen, X. Liu, J. Chen, *J. Am. Chem. Soc.* **2016**, *138*, 12894.
- [75] B. Kakoty, R. Vengarathody, S. Mukherji, V. Ahuja, A. Joseph, C. Narayana, S. Balasubramanian, P. Senguttuvan, *J. Mater. Chem. A.* **2022**, *10*, 12597.

Manuscript received: May 14, 2025

Revised manuscript received: July 31, 2025

Version of record online: